Article

Transient Permeabilization of Living Cells: Combining Shear Flow and Acoustofluidic Trapping for the Facilitated Uptake of Molecules

Andrej Kamenac [1,2,†], Felix L. Schilberth [1,†], Ernst Wagner [2,3], Achim Wixforth [1,2], Ulrich Lächelt [2,3] and Christoph Westerhausen [1,2,4,*]

1   Experimental Physics I, Institute of Physics, University of Augsburg, 86159 Augsburg, Germany; andrej.kamenac@physik.uni-augsburg.de (A.K.); felix.schilberth@kabelmail.de (F.L.S.); achim.wixforth@physik.uni-augsburg.de (A.W.)
2   Center for NanoScience (CeNS), Ludwig-Maximilians-Universität München, 80799 Munich, Germany; ernst.wagner@cup.uni-muenchen.de (E.W.); ulrich.laechelt@cup.uni-muenchen.de (U.L.)
3   Pharmaceutical Biotechnology, Department of Pharmacy, Ludwig-Maximilians-Universität München, 81377 Munich, Germany
4   Physiology, Institute of Theoretical Medicine, University of Augsburg, 86159 Augsburg, Germany
*   Correspondence: christoph.westerhausen@gmail.com
†   Equally contributing authors.

Abstract: Here, we present a novel approach for the transient permeabilization of cells. We combined laminar shear flow in a microchannel with chaotic advection employing surface acoustic waves. First, as a fundamental result on the one hand, and as a kind of reference measurement for the more complex acoustofluidic approach on the other hand, we studied the permeabilization of cells in pure shear flow in a microchannel with Y-geometry. As a proof of principle, we used fluorescent dyes as model drugs and investigated their internalization into HeLa cells. We found that drug uptake scaled non-linearly with flow rate and thus shear stress. For calcein, we obtained a maximal enhancement factor of about 12 at an optimum flow rate of $Q = 500$ μL/h in the geometry used here compared to static incubation. This result is discussed in the light of structural phase transitions of lipid membranes accompanied by non-linear effects, as the plasma membrane is the main barrier to overcome. Second, we demonstrated the enhanced permeabilization of acoustically trapped cells in surface acoustic wave induced vortices in a microchannel, with an enhancement factor of about 18 compared to quasi-static incubation. Moreover, we optimized the trapping conditions regarding flow rate, the power level of the surface acoustic wave, and trapping time. Finally, we showed that our method is not limited to small molecules but can also be applied to compounds with higher molecular weight.

Keywords: drug delivery; permeabilization; surface acoustic waves; acoustic trap; chaotic advection; microfluidics; acoustofluidics; calcein; FITC-dextran; GFP; structural phase transition; pore

1. Introduction

Intracellular delivery is a major mutual challenge for various applications, like cell-based therapies, gene editing, the induction of pluripotent stem cells, and intracellular probes. Existing strategies to overcome the main barrier—the membrane—have been extensively reviewed by Stewart et al. [1]. Most carrier-mediated biochemical approaches are elaborate and require detailed knowledge about the molecular targets, and therefore do not offer a general solution for the cell-based screening of agent libraries.

Usually, physical approaches are carrier-free and directly penetrate the plasma membrane or induce the opening of transient pores. A common method, electroporation, applies electrical fields to open the pores, which then enable diffusion of the cargo molecules into the cell [2]. This permeabilization process leaves the cell in a vulnerable state immediately

after treatment, as it influences the electrochemical equilibrium. The ionic composition of the cytoplasm is particularly affected, which in the end can lead to apoptosis [3,4]. However, this generally undesired effect can be applied, for example, in direct tumor treatment [5,6].

Instead of targeting electric membrane characteristics, another possibility is based on addressing mechanical membrane properties. Sonoporation methods expose cells to ultrasound in the range of $f = 20$ kHz to $f = 10$ MHz, which is useful for various applications. In clinical therapies, ultrasound is used, for example, for clot lysis in blood vessels, the stimulation of bone fracture healing, and tumor treatment [7]. For drug delivery purposes, sonoporation is supposed to open pores in the plasma membrane by microfluidic cavitation and implosion [8]. As the occurrence of these cavitations is rather rare in liquids, one drawback of these methods is the low effectiveness if they are applied without ultrasonic contrast agents, as, for example, microbubbles [9,10]. Newer contrast agent free sonoporation methods achieve high throughput at a high cell viability [11].

A fluid–mechanical approach utilizes flow-induced shear forces to form pores. Flowing water molecules can, e.g., cause buckling instabilities in the lipid bilayer and open pores [12]. Defined shear forces are achieved in microfluidic channels, where a parabolic velocity profile results in a linear shear profile. Furthermore, a constant shear profile can be realized in shearing disc viscosimeters in the plate-cone geometry, and have been found to enhance cell permeabilization [13]. These approaches come with low Reynolds numbers, indicating a highly laminar flow.

Further fluid–mechanical impact, using methods from solid state physics and rf-engineering, has been reported by Ramesan et al. [14,15]. They use surface acoustic waves (SAW) as a tool to generate oscillating acoustic pressure to act on cells. In their study, cells were not directly exposed to surface acoustic waves, as a couplant fluid and a well plate with a glass bottom were used. This method is suitable for a limited number of adherent cells due to the design limitations of the interdigital transducer and the liquid environment. Even though it was not discussed in their study, the parameters used are known to induce shear flow due to acoustic streaming, especially at high powers [16–19].

In our approach, presented here, we combined laminar shear flow with chaotic advection employing SAW. This enabled the trapping of suspended cells in vortices within a continuous fluid stream in a microchannel to overcome the drawbacks of the previous concepts. The microfluidic framework enables precise spatial and temporal control of the applied SAW. The SAW coupled directly into the fluid and induced two vortices, which mixed two fluids in a Y-shaped microchannel, inspired by the mixing concept reported earlier [17,20,21]. In combination, an oscillating acoustic pressure and shear forces were applied to the cells, as well as chaotic advection [21]. As a proof of principle, we used impermeable fluorescent dyes as model drugs and investigated their internalization into HeLa cells. Future studies should examine the potential to scale it up to a high-throughput setup, and additionally address transfection.

The structure of this paper is as follows. First, we introduce the experimental design and methods. Second, we present a non-linear permeabilization by pure shear flow. Third, we present the enhanced permeabilization of acoustically trapped cells in SAW-induced vortices before we subsequently optimize the trapping conditions. Finally, we show that our method is not limited to small molecules but can also be applied to compounds with higher molecular weight.

2. Methods and Materials

A schematic illustration of the whole setup and treatment process is shown in Figure 1a. The setup consists of a SAW chip, comprising an interdigitated "slanted" or "tapered" transducer for the generation of SAW and a Y-shaped microchannel. This channel is oriented perpendicular to the SAW path. In the channel, laminar flow limits the mixing of the two fluids to a diffusion-driven process at the interface. At the site of the active interdigital transducer (IDT), SAW are created and lead to mixing by chaotic advection

as reported earlier [21]. The SAW-induced acoustic mixing folds the streamlines and establishes contact between cells and dye, and simultaneously permeabilizes the cell membrane. Subsequently, after passing an outlet tube, the cells are collected in a well plate and analyzed by fluorescence microscopy after incubation to allow for adhesion.
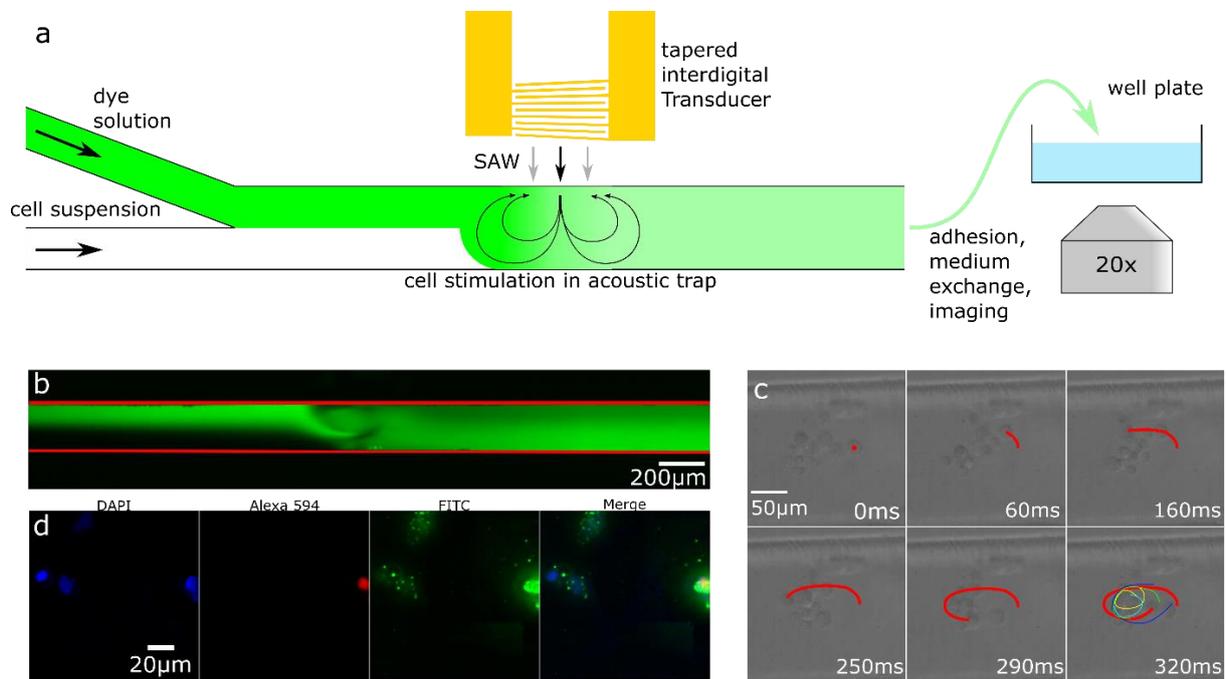
Figure 1. (**a**) Illustration of the acoustofluidic delivery setup. The cell suspension (white) and the dye solution (green) meet at the Y-shaped junction. At the active TIDT sites (gray and black arrows), SAW couple into the liquid and mix effectively by forming two vortices. The spatial position of the SAW changes by adjusting the RF frequency. The dye–cell suspension travels via tubing into a well plate. A two-hour adhesion period, dye-rinsing protocol, and fluorescence imaging follows: (**b**) fluorescence image of calcein in the channel. The fluorescent dye and cell suspension are mixed close to the TIDT site; (**c**) phase contrast image time series of HeLa cells trapped in SAW-induced vortices. The lines highlight the trajectories in the vortices. (**d**) Typical recorded images in the different fluorescent channels (DAPI/Alexa 594/FITC).

Figure 1b shows a fluorescence micrograph, visualizing the laminar flow at the beginning of the channel and the mixing process at the SAW interaction region. Further downstream, the dye is distributed evenly over the whole width of the channel. During the treatment, the power of the SAW remains constant, while the frequency is slightly varied in order to shift the position of the SAW-induced vortices, as indicated in Figure 1a. This leads to cell trapping, as shown in Figure 1c. The lines highlight the trajectories of some of the cells. The spatially shifting vortices are caused by three subsequently applied signals with increasing frequencies (f = 80.3–81.3–82.3 MHz), each for a defined time period, e.g., t_{step} = 20 s, resulting in a SAW cycle duration of $t_{SAW} = 3 \cdot t_{step}$ = 1 min. As the vortices shift from left to right, the trapped cells are shifted spatially, too. When the last frequency is about to change back to the first, all cells are released from the trap. However, a few cells are released stochastically from the trap at shorter time scales. This frequency program and the trapping feature result in a constant distribution of net treatment times ranging from t = 0 s to t = 60 s, as cells are flowing into the single trap continuously.

2.1. Cells and Cell Culture

HeLa cells (ATCC® CCL-2™) were cultured in Nunc Delta surface culture flasks (Nunc A/S, Roskilde, Denmark) at c = 5% CO_2, c = 95% humidity, and T = 37 °C containing V = 5 mL of cell medium (DMEM, FBS, and streptomycin/penicillin (all Biochrom, Berlin, Germany) in the ratio 500:50:5). The cell cultures were split every 3–4 days using a Trypsin–EDTA solution (c = 0.025%, Sigma-Aldrich, St. Louis, MI, USA).

2.2. SAW Chip

The SAW chip was manufactured using a tapered interdigital transducer (TIDT) on a piezoelectric $LiNbO_3$ (128° rot Y-Cut) substrate (Roditi International Corporation Ltd., London, UK) [22] with a standard photolithography process and consists of three metal layers (Ti–Au–Ti, height h = 5 nm$-$50 nm$-$5 nm). For protection of the multifinger-structure, the production was finished with a layer of SiO_2 with a height of h = 150 nm.

The TIDT provides a continuous frequency range between f = 79–83 MHz, which was analyzed using a vector network analyzer (Rohde & Schwarz ZVC 20 KHz$-$8 GHz Vector Network Analyzer, Rohde & Schwarz, Germany). The frequency spectrum allowed for the creation of acoustic streaming at various continuous positions. However, we exclusively used three distinct frequencies: f_1 = 80.3 MHz, f_2 = 81.3 MHz, and f_3 = 82.3 MHz. The TIDT activation was controlled by a CellEvator (Advalytix, Munich, Germany) and contacted with SMA connectors on a circuit board and high frequency wiring. The control was yielded by a custom-built LabView program (National Instruments, Austin, TX, USA), enabling the regulation of SAW power (p) up to the required maximum of p = 30 dBm, as well as time-controlled frequency adjustment.

2.3. Microfluidic Channels

The microfluidic channels were produced by employing a standard soft lithography process [23]. Consisting of polydimethylsiloxane (PDMS) (Dow Corning, Midland, MI, USA), the Y-shaped geometry is formed by two inlets, each with a cross section of A = 100 × 100 μm^2, which merge into a main channel with A = 200 × 100 μm^2. Approximately x = 450 μm downstream from the junction, the PDMS block contains a recess in which the TIDT precisely fits in. The microfluidic channel is finally sealed by pressing the PDMS on the SAW chip by a holder.

2.4. Acoustofluidic Permeabilization

The acoustofluidic delivery method resembles a microfluidic mixing process similar to that described in [20]. One inlet is injected with the cell suspension (in medium), and the other one is injected with a calcein solution at a concentration of c = 0.2 mg/mL in PBS (pH = 7.4, Biochrom, Berlin, Germany). Calcein (m_U = 622.54 Da) is almost impermeable to the cell membrane by simple diffusion [24] at the used timescales, and is therefore suited as a model drug in these experiments. In additional experiments, solutions of FITC–dextran (m_U = 10 kDa, Sigma-Aldrich Chemie GmbH, St. Louis, MI, USA) and eGFP (produced by recombinant bacterial expression [25]) at a concentration of c = 0.2 mg/mL were used.

After treatment, the cells were transferred via a tubing (inner diameter $\varnothing$ = 389 μm, Pro Liquid GmbH, Überlingen, Germany) of a length of about l = 9.3 cm into a well plate containing V = 200 μL cell medium. At this point, the effective cell treatment ends, as the dye concentration is diluted. Finally, a two-hour cell adhesion period prevents the cells from detaching while subsequently exchanging the fluorescent supernatant several times.

2.5. Data Processing

For data acquisition, the cells were fluorescently labelled using the ThermoFisher ReadyProbes™ Cell Viability Imaging Kit Blue/Red (Thermo Fisher Scientific, Invitrogen, Waltham, MA, USA), which labels the cell nuclei and highlights dead cells. A fluorescence microscope (Axiovert 200 M, Carl Zeiss Microscopy, Jena, Germany) was used to image three channels. Figure 1d shows such an image series of the different channels and their merge. The first image shows the nuclei of all visible cells. Subsequently, the Alexa 594 image identifies dead cells, and the FITC image shows the calcein fluorescence. A closer examination reveals both—uptake into the cytoplasm, indicated by the homogenous foggy green, and an endocytotic accumulation, indicated by the intracellular distribution of bright, sharp spots. The merge of all three images contains all of the data necessary to

analyze the outcome of the experiments regarding statistical information, as well as the intensity as a quantitative measure of dye uptake.

The analysis of these experiments was performed using a custom-made MATLAB script (The MathWorks Inc., Natick, MA, USA). Using the DAPI image, all cell nuclei were identified regarding their size and location and dilated by a factor of two by the algorithm. This compensates for the exact determination of the cell area via light microscopy, which is often ambiguous. Via the Alexa 594 channel, dead cells were identified and excluded from the analysis. Subsequently, the integrated intensity was analyzed in the FITC channel. This evaluation method might, however, slightly underestimate the dye uptake, as the nucleus dilation-dependent intensity integration does not always cover the whole cell.

2.6. Particle Image Velocimetry

For the characterization of the flow pattern in the microchannel, particle image velocimetry (PIV) experiments were performed. For this method, $\varnothing$ = 4.5 μm polystyrene beads (Polybead[®], Polysciences, Inc., Warrington, PA, USA) were suspended and pumped through the system. These particles follow the streamlines and are small enough not to disturb them. In this setup, videos were recorded with a high-speed camera (Photron UX, Photron Inc., San Diego, CA, USA) at a framerate of 1000 images per second. From these videos, 300 frames were analyzed with the MATLAB app PIVlab [26], yielding the velocity distribution of the particles in the channel. With this information, further parameters, such as the shear rate, can be extracted. The parameters used for the PIV experiments were a flow rate of Q = 80 μL/h and a SAW input power of p = 28 dBm.

3. Results and Discussion

3.1. Shear Flow Induced Permeabilization without Acoustic Trapping

To separate between permeabilization by pure shear flow as reported by Clarke et al. [27] and permeabilization by SAW, we quantified the shear flow induced permeabilization of HeLa cells in an identical setup but without employing SAW. Figure 2 shows the influence of shear and friction forces caused exclusively by channel geometry on the permeabilization over a wide range of flow rates and thus shear forces.

As the schematic in Figure 2a indicates, the cells were exposed to shear stress within the microchannel without bulk contact with the dye. Two mechanisms drive the mixing of the cell suspension and the fluorescent dye solution. The first mechanism is diffusion, which is predominant at the interface of the fluids in the microchannel. The second mechanism is Dean flow, which is predominant around the high curvature at the outlet, consisting of the microchannel–tubing intersection [28]. However, diffusion-driven mixing in comparison to Dean flow mixing is negligible due to the low efficiency and short time span.

The uptake increases roughly linearly for low flow rates up to Q = 500 μL/h. For further increasing flow rates, the uptake decreases. At Q = 1500 μL/h, the uptake is comparable to quasi-static conditions at Q = 50 μL/h. Earlier reports claim a linear relationship between shear stress and permeabilization [13]. However, Figure 2b shows a clearly non-linear relationship. This could lead to the trivial hypothesis that the constant length of the outlet tube limits the effective incubation time (exposure to calcein before dilution in the well plate), and thus the quantified uptake. To account for the variation of contact time as function of flow rate, Q, in Figure S1, we rescale the original values with a contact time dependent scaling factor. The non-linearity with a pronounced maximum is conserved for these corrections.
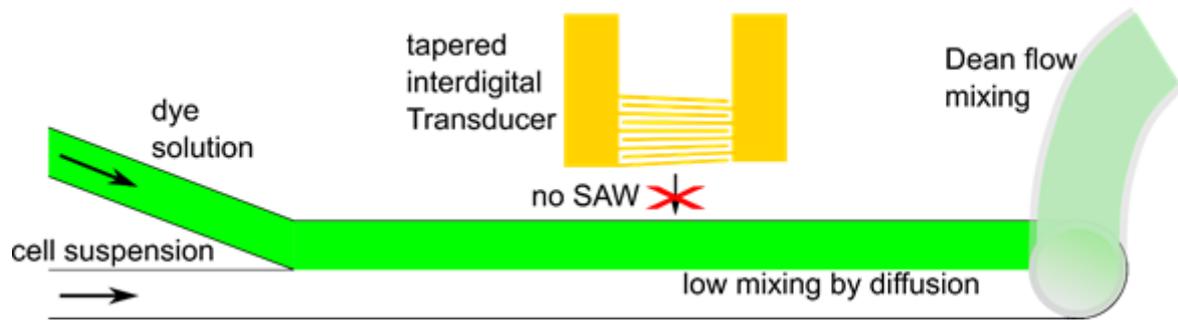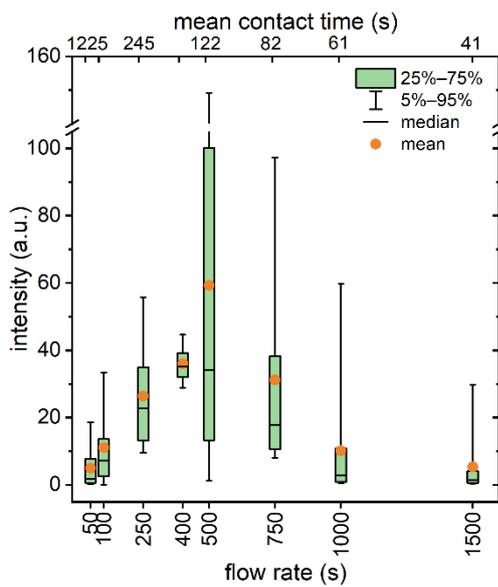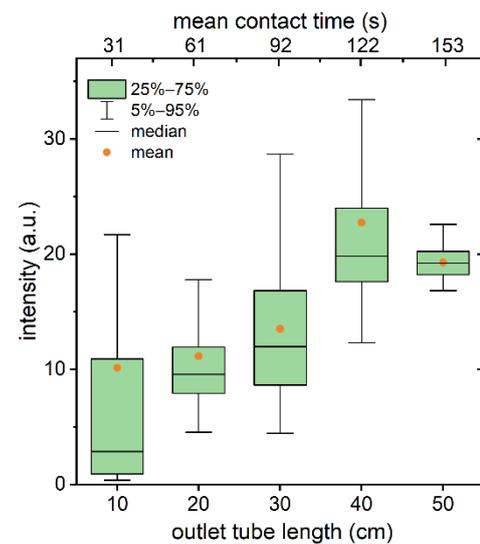
Figure 2. Flow rate and contact time dependent dye uptake. (**a**) The schematic illustrates the general setup. Note that here, no SAW is applied, and mixing appears at the microchannel–tubing intersection subsequent to permeabilization by shear stress in the channel. (**b**) The dye uptake rises linearly and shows a pronounced maximum at 500 μL/h, and then quickly decreases. (**c**) Reference measurement to determine the impact of the outlet tube length (and therefore contact time). As a mean for each box, *n* = 163 cells have been analyzed for each boxplot in Figure 2b and *n* = 397 cells have been analyzed for each boxplot in Figure 2c.

In addition to the calculation, we test this hypothesis experimentally. Therefore, we perform additional reference experiments at a flow rate of $Q = 1000$ μL/h and an outlet tube length of $l = 20$ cm, and vary the contact time by variation of the length, l, of the outlet tube (Figure 2c). Indeed, increasing the outlet tube length leads to increased dye uptake for this high flow rate. Nevertheless, this does not exceed a factor of two in dye uptake, what is consistent with the theoretical estimations shown in Figure S1.

Therefore, our findings hint towards a diffusive uptake mechanism, as would be expected for uptake through membrane pores as shown in an earlier study using a stenosis in a microfluidic channel [29]. The authors of that study found saturation behavior, where 70–90% of the total uptake happened in the first minute after stimulation. In our study, for an outlet tube length of 40–50 cm, the dye uptake saturates (see Figure 2c), most likely due to the resealing of the pores, as observed in [29]. Strikingly, using the mean flow velocity and an outlet tube length of $l = 40$ cm results in a mean cell–dye contact time of 122 s in our setup, which differs from the earlier reported value only by a factor of two. Considering that the majority of the cells travel around the center of the tube due to non-inertial lift forces [30], with a velocity close to twice the mean velocity, the difference vanishes.

To test the reversibility of flow rate dependent permeabilization, we performed the same experiment as in Figure 2b, but pretreated the cells beforehand, as illustrated in Figure 3a. For the pretreatment, we pumped the cell suspension at a very high flow rate of $Q = 4000$ μL/h through the microchannel to activate the permeabilization mechanism, presumably the formation of pores. Afterwards, the very same cells were then aliquoted and used for an experiment as in Figure 2b. The results are shown in Figure 3b. Again, for a flow rate of $Q = 500$ μL/h, a distinct maximum appears (as shown in Figure 2b) without pretreatment. Due to some technical equipment differences, the quantitative dye uptake in total appears somewhat lower.
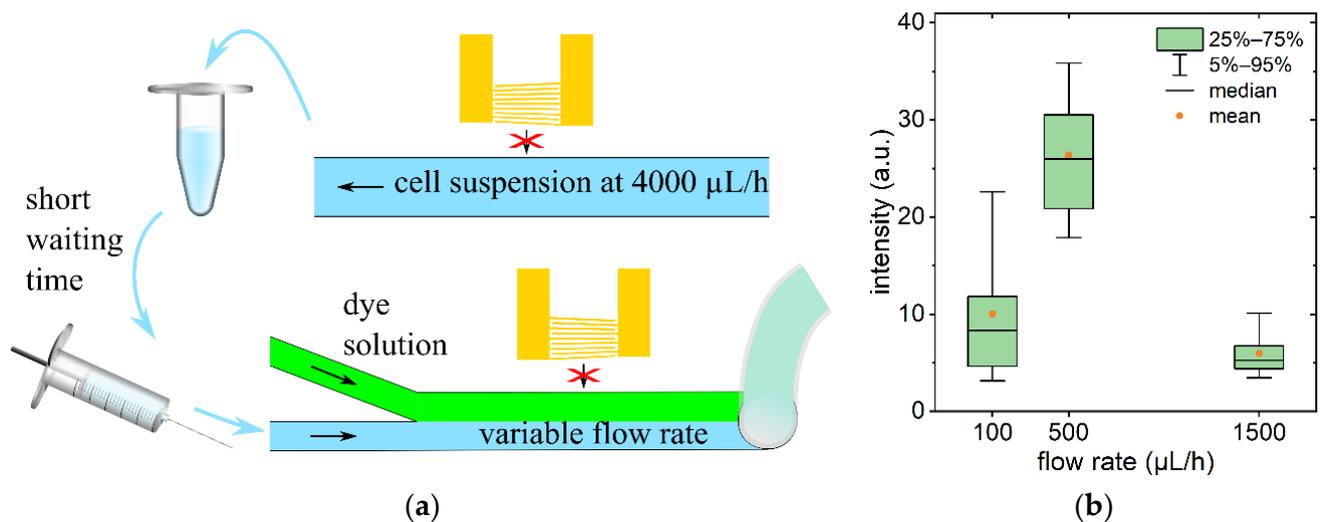
Figure 3. Flow rate dependent dye uptake of cells pretreated at a high flow rate of Q = 4000 μL/h. (**a**) Schematic experimental setup and (**b**) results. As a mean for each box *n* = 326 cells have been analyzed.

This strongly suggests a transient pore forming mechanism with an optimum dye contact time due to a limited pore lifetime. This pore formation must depend on the thermodynamic membrane state and thus also on mechanical stimulation. This is not limited to the application of passive shear forces resulting from the channel geometry and flow rate, but could also be extended to temperature mediated changes in the membrane state. Another indication that is in line with this interpretation is the fact that at the flow rate of maximal uptake (compare Figure 2), we observe a high variability of dye uptake. This could be the result of a narrow window in the cell membrane state diagram. However, in the following experiments, we upgrade the complexity of mechanical stimulation by employing SAW with cell trapping vortices and the corresponding pressure fluctuations. Here, the permeabilization and exposure to high dye concentrations happens at the same time.

3.2. Acoustofluidic Trapping and Stimulated Uptake Employing Surface Acoustic Waves

As illustrated and shown in Figure 1a, launching SAW in the microchannel creates vortices that trap cells for a distinct time, while a constant stream of dye solution passes the cells. The three main adjustment parameters are SAW power level, p, flow rate, Q, and SAW cycle duration, t_{SAW}. In the following experiments, we first vary p and Q and show how these two parameters are related, before we then study the SAW cycle duration, t_{SAW}.

Figure 4a shows the uptake determined in experiments with a flow rate of $Q = 100$ μL/h as function of SAW power level, p. For this flow rate, power levels up to $p = 28$ dBm do not result in significantly enhanced uptake. For $p = 29$ dBm, the uptake is enhanced compared to the pure flow reference (Figure 2b, $Q = 50$ μL/h, no SAW) by a factor of 18 with a large width of the uptake distribution. This width arises from the chaotic

nature of the method, as various factors were not or cannot be fully controlled, such as dwelling time in the trap, exact occupied streamline in the vortex, and thus shear stress.


(a)

(b)
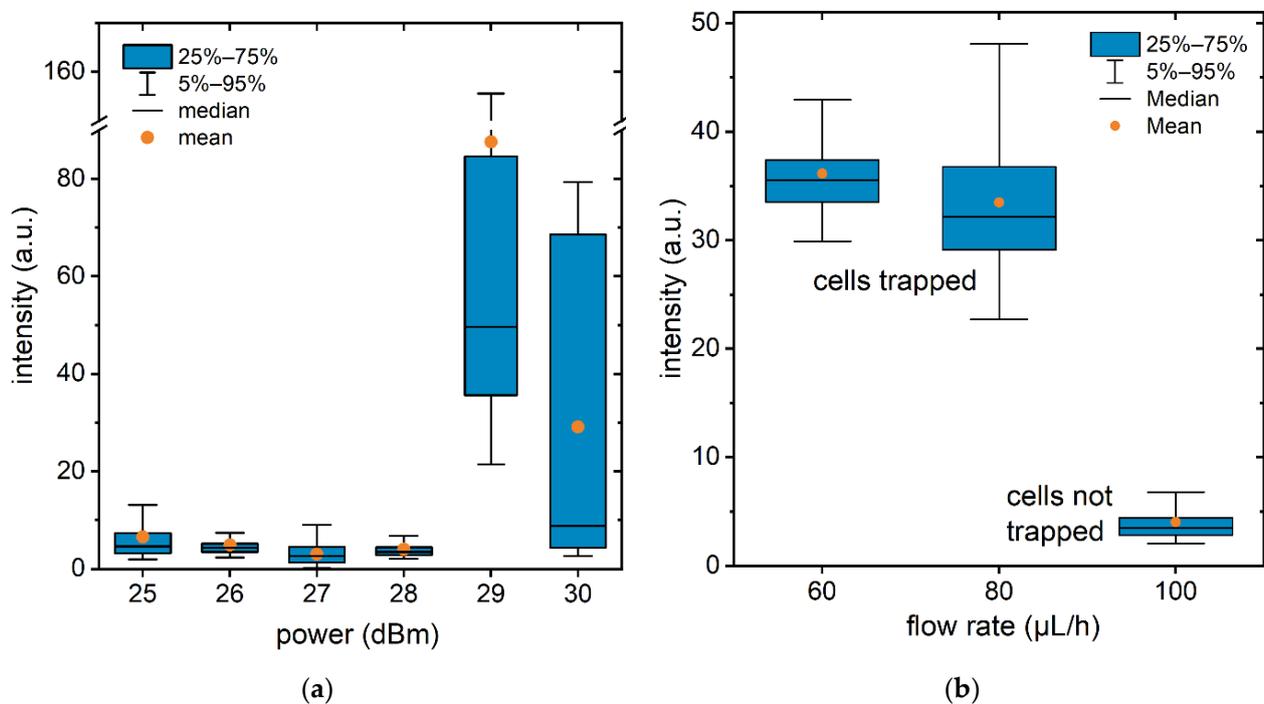
Figure 4. (a) Uptake as a function of SAW power (at Q = 100 μL/h, t_{SAW} = 1 min). A local maximum is clearly visible at p = 29 dBm. Higher powers promote cell death. (b) Uptake as a function of flow rate (p = 28 dBm). While significant uptake is achieved for a flow rate of Q = 80 μL/h and below, no increased uptake is achieved for a flow rate of Q = 100 μL/h. This can be understood by the flow rate and power dependent trapping capability of the vortices (see main text). As a mean for each box, n = 385 cells have been analyzed for each boxplot in Figure 4a, and n = 574 cells have been analyzed for each boxplot in Figure 4b.

At p = 30 dBm, the uptake decreases again. This high power also promotes cell death (mean cell density is decreased by a factor of 13 compared to p = 29 dBm). The narrow suitable power level range is a function of the flow rate, Q. This can be understood by a flow rate dependent trapping capability for a constant power level. Along the same lines as shown for the mixing efficiency in a similar setup, the higher flow rates here require higher power for trapping [20]. In an earlier publication, we showed that the SAW-driven flow component perpendicular to the channel direction must be roughly the same as the flow component downstream along the channel axis. Thus, for power levels below p = 29 dBm, where SAW are activated but cells are not trapped in the vortices, the cells mainly experience pure shear flow, as the quantified uptake is roughly the same in both cases.

To test this hypothesis, we reduced the flow rate to a constant power of p = 28 dBm. Figure 4b shows dye uptake at the flow rate of Q = 80 μL/h (which is eight times higher than the uptake at Q = 100 μL/h), which quantitatively matches the enhancement factor derived from Figure 4. For further experiments, we then applied these values of power; a flow rate of p = 28 dBm and Q = 80 μL/h for a gentler treatment.

In the following, we quantify the velocity and shear profile of the SAW-induced vortices, employing particle image velocimetry, before elucidating the role of SAW cycle duration for permeabilization.

Figure 5 visualizes the flow field with and without SAW application. Without SAW application, a maximal shear rate of about $\dot{\gamma} = 30\frac{1}{s}$ is achieved. This is in line with theoretically calculated shear rates assuming a parabolic flow profile.
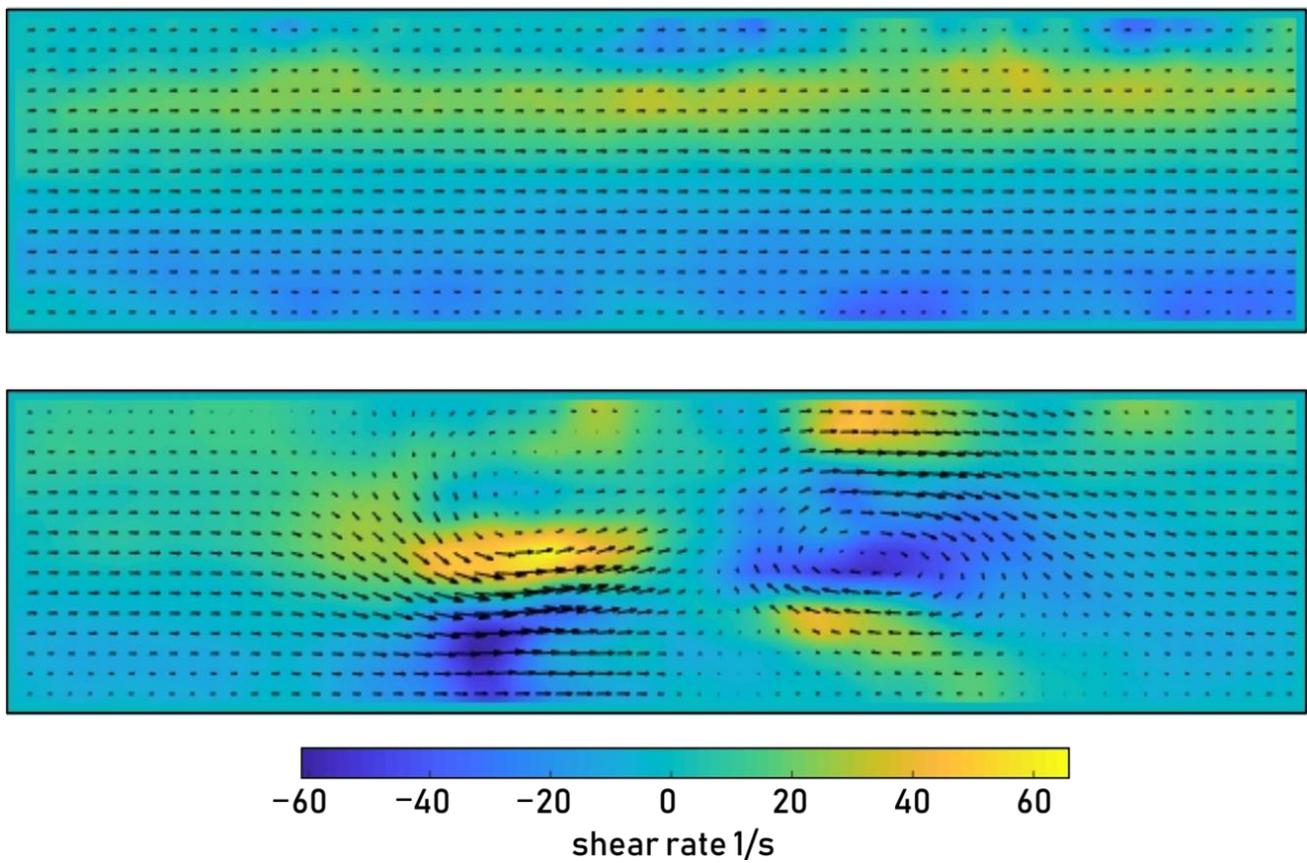
Figure 5. PIV measurements of the flow fields in the microchannel without (**top**) and with (**bottom**) activated SAW ($Q = 80\ \mu L/h$, $p = 28$ dBm). The arrows indicate the velocity field, whereas the color indicates the shear rate within the x–y plane. Two SAW-induced vortices appear (**bottom**), and maximal shear rates are roughly increased by a factor of two. Note that the z-component of the flow field is not included here.

As soon as the SAW is applied, the symmetry of the shear field is broken, and the maximum shear rate is increased by a factor of at least two. Here, two vortices are visible, in which the shear rate is maximal. As the cells are trapped in these vortices, they are continuously stimulated by these higher shear forces, leading to improved uptake behavior. This stimulation might be comparable to reports of a model system, where giant unilamellar vesicles under tension show drastically improved pore lifetimes. Although we do not increase tension directly, shear forces deform the spherical shape (Taylor deformation), which results in a rise in tension [31]. The origin of the increase of uptake by SAW is partially explained by the two-fold increased shear rate. In part, it might be underestimated, as the SAW-treated cells also experience shear stress in the z-direction, however, the shear profile evolution in z-direction can be seen in Figure S2. Another contribution is expected to arise from the dye–cell contact time, which will be investigated in the following experiment.

3.3. SAW Cycle Duration

To clarify terminology, the SAW cycle duration (t_{SAW}) is the total time for the SAW vortices to sweep through the three frequencies and therefore three spatial positions. This results in a mean dwell time, t_d, where the cells are trapped in the vortex, which is generally equally distributed between $t_d = 0$ s and the SAW cycle duration, t_{SAW}. We quantified the optimal SAW cycle duration and varied this parameter at a flow rate of $Q = 80\ \mu L/h$ and a SAW power level of $p = 28$ dBm. The results are shown in Figure 6. With increasing t_{SAW}, and thus treatment time, the uptake rises linearly until it reaches a maximum for $t_{SAW} = 2$ min. Extremely short t_{SAW} results in an uptake close to the reference ($Q = 50\ \mu L/h$, no SAW, see Figure 2a). This results in an enhancement factor for the uptake of $f_{SAW} \approx$

13. For $t_{SAW} > 2$ min, the dye uptake decreases again. Since the increased SAW cycle duration also induces higher cell death (resulting mean cell density in the analyzed well at $t_{SAW} = 6$ min is decreased by a factor of four compared to $t_{SAW} = 2$ min), the low dye uptake might be explained by the selection of surviving (less permeabilized) cells. This therefore suggests a tradeoff between increasing dye uptake for high trapping times and increasing cell death for even higher trapping times.
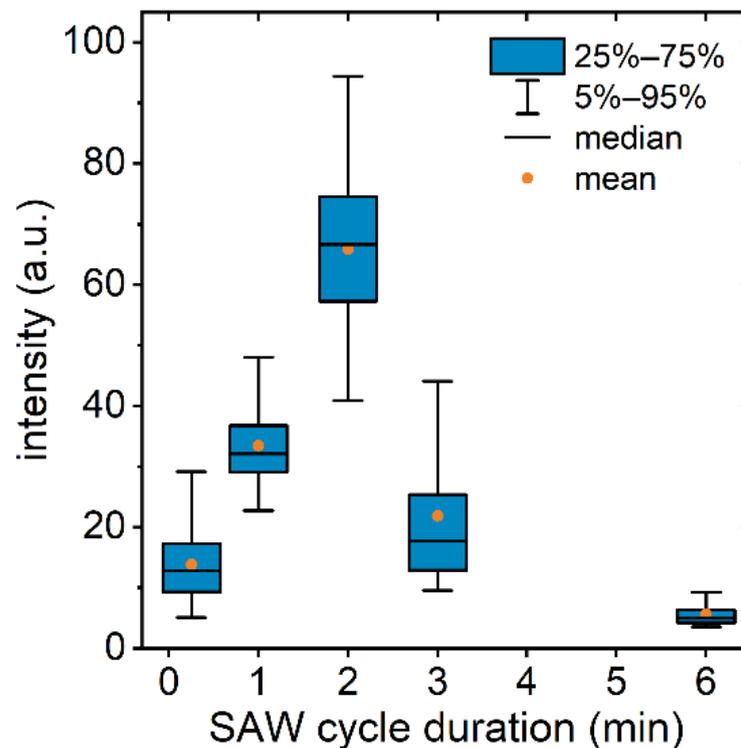
Figure 6. Boxplots of fluorescence intensity (calcein) as a function of SAW cycle duration ($Q = 80$ μL/h, $p = 28$ dBm). As a mean for each bo, $n = 758$ cells have been analyzed.

As described above, $t_{SAW} = 2$ min is equivalent to a mean dwell time $t_d = 1$ min. This optimum for t_d agrees well with the saturation of the dye uptake as a function of the contact time in pure shear flow, as depicted in Figure 2 and as observed in literature [29].

To narrow down the main contributions resulting in the increased uptake, we need to examine the experimental differences caused by additionally launching the SAW. First, the wave is accompanied by an oscillating electrical field, with field strengths as high as $E = 10^4$ V/m due to the piezoelectric substrate. Even though this was discussed as a major influencing factor earlier [14], due to shielding effects by ions in the fluid, we estimate this as a minor contribution, as the penetration depth (Debye length) can be calculated to be at the order of $\lambda_D = 1$ nm [32].

Second, the effective exposure time, t_{exp}, of the cells to high shear rates is largely enhanced by the dwell time in the vortices. The effective exposure time to shear stress is about $t_{exp} \approx 6.9$ s (flow time in the microchannel) without SAW, and about $t_{exp} \approx 6.9 + 60$ s with SAW ($t_{SAW} = 2$ min). This increased exposure to higher shear rates increases the energy input into the membrane and can lead to a new equilibrium number of transient pores [33]. Finally, in pure laminar flow experiments, a dye depletion zone close to the membrane might appear due to diffusion to some extent. In contrast, with SAW application, the permeabilized cells are moved along their trajectories in the vortices through the dye solution, which might result in an artificially increased diffusion constant and thus a reduction of the depletion zone at the membrane. However, we cannot discriminate between increased permeability due to longer shear stress exposure and removal of the diffusion limitation and do not further quantify these effects here. Nevertheless, this

experiment provides the optimal combination of flow rate, power, and SAW cycle duration as a suitable parameter set for gentle cell membrane permeabilization. At this point, the exciting question remains whether the presented delivery method also holds for larger molecules like dextrans or proteins.

3.4. Applicability for Various Molecular Weights

We tested three fluorescent model compounds of different molecular weight, spanning almost two orders of magnitude: calcein (m_U = 0.6 kDa), FITC–dextran (m_U = 10 kDa), and eGFP (m_U = 27 kDa). To account for different ratios of molar mass at constant mass concentration, we normalized the measured fluorescence intensity to the mass according to the data shown in Table 1.

Table 1. Fluorescence intensity of the used fluorescent compounds at c = 0.2 mg/mL normalized to the intensity of the calcein solution.

Fluorescent Species	Brightness
Calcein	1
FITC–dextran	0.12
eGFP	0.46

Figure 7 shows the uptake in HeLa cells for four different treatments at a given model compound mass concentration of *c* = 0.2 mg/mL: calcein under flow (no SAW), calcein under SAW treatment, FITC–dextran under SAW treatment, and eGFP under SAW treatment. For the two latter model compounds, the mass uptake in static incubation references was quantified. The mass uptake for SAW-treated cells was increased by about six-fold for calcein compared to pure flow treatment (*Q* = 100 µL/h).
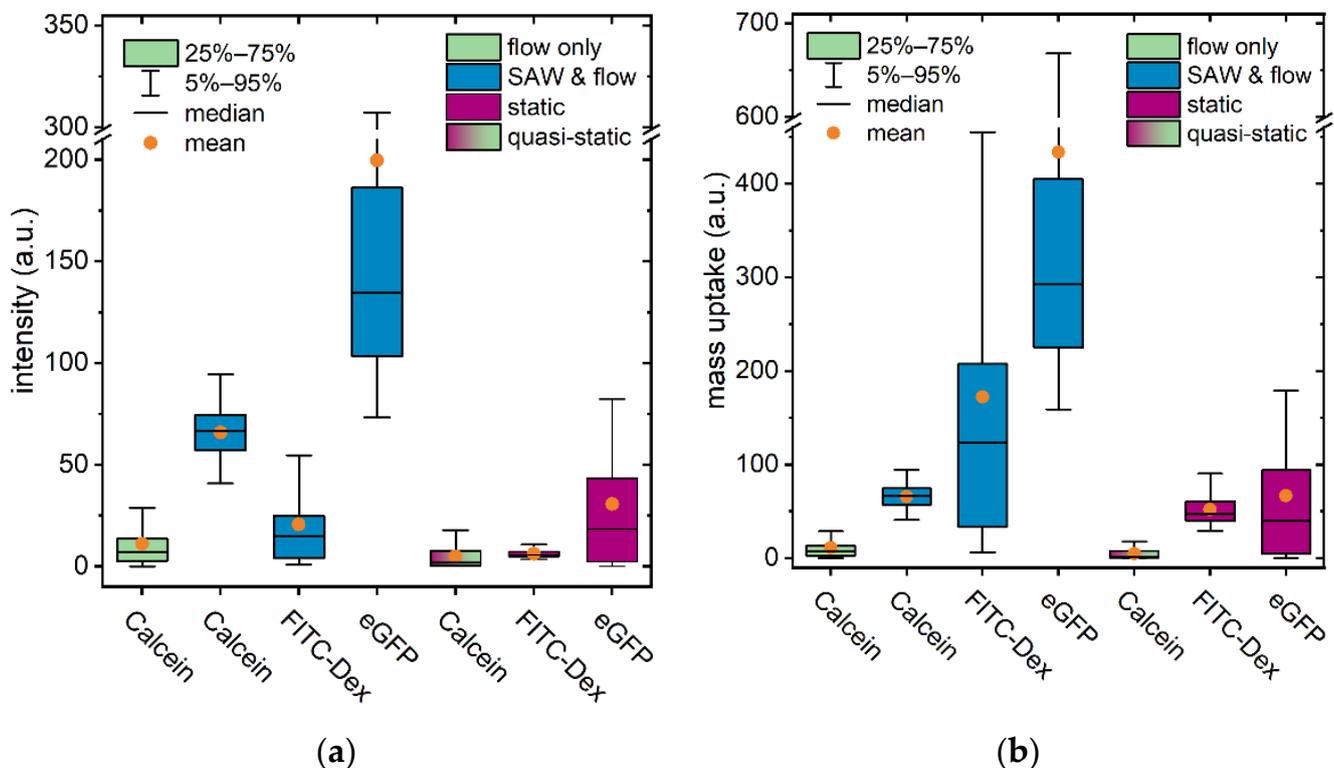
Figure 7. Absolute incorporated dye intensity for different cell treatments. (**a**) Raw data. (**b**) Data normalized to mass brightness according to Table 1. The normalization to brightness uses the inverse measured relative intensities as listed in Table 1.

This agrees well with Figure 4b, where the enhancement factor is about $f_{SAW} \approx 8$, as described before. However, in Figure 4a, the enhancement factor is about 18 when comparing the optimal SAW power treatment to the low power treatments, which are the closest to pure flow conditions. These two experiments were conducted with slight variations: $Q = 100$ µL/h, $p = 29$ dBm, and $t_{SAW} = 1$ min (Figure 4a) vs. $Q = 80$ µL/h, $p = 28$ dBm, and $t_{SAW} = 2$ min (Figure 4b). Consequently, the enhancement factor here is about a factor of two lower, which matches the influence of the cycle duration as shown in Figure 6.

In further comparison of the SAW treatment to static conditions, the mass uptake of calcein is enhanced by a factor of 18 (Figure 7), whereas pure flow without SAW application at the same flow rate enhances the uptake by a factor of five (Figure 7). However, as Figure 6 suggests, choosing $t_{SAW} = 2$ min instead of $t_{SAW} = 1$ min (Figure 4a) could potentially result in an additional doubling of uptake efficiency to a factor of up to 36.

The uptake of FITC–dextran is increased about three-fold compared to the static reference, while the corresponding uptake of eGFP is increased 6–7-fold; in this result, it has not yet been considered that the diffusion coefficient varies for the different dyes. The diffusion coefficient, D, is estimated using the Stokes–Einstein equation, and it is calculated to be $D = 3.3 \times 10^{-10}$ m^2/s for calcein [34], $D = 1.1 \times 10^{-10}$ for FITC–dextran, and $D = 1.0 \times 10^{-10}$ for eGFP. According to Fick's diffusion law, as diffusion is linearly dependent on the diffusion coefficient, calcein is more likely to diffuse through an open pore than eGFP or FITC–dextran by a factor of three. Taking this into account, the findings of higher uptake for higher molecular masses intensify.

Surprisingly, the enhancement factors do not obviously correlate with molecular weight. For the hypothesized facilitated uptake by pore formation, the hydrodynamic diameter, d_h, might be more important. Here, d_h does not scale linearly with m_u, as 10 kDa FITC–dextran has a more rod-like geometry in contrast to the folded 27 kDa eGFP. Taking the diffusion coefficient into account, the enhancement in uptake factors for calcein and eGFP (the non-rod-like cases) match very well at $f_C = 18$.

Most importantly, the data shows that the presented delivery method is not limited to small molecules, but also works for larger sugars and proteins.

4. Conclusions and Outlook

In summary, we presented a simple method for the vector-free permeabilization of suspended living cells. This method is based on shear flow and acoustic trapping of suspended cells on a chip. Both shear flow and acoustic trapping permeabilize suspended cells. Acoustic trapping is accompanied by the folding of the streamlines (vortices). We propose a transient pore forming mechanism to govern the permeabilization, which is reversible by pore sealing after a lifetime of about $t_{pore} = 1$ min. Our acoustofluidic setup provides the possibility to control a complex flow field, which is spatially and temporally switchable.

On the fundamental side, we quantified the dye uptake for pure shear flow permeabilization and found a nonlinear relationship. This can be explained by pore formation. External forces like shear stress lead to a stretching of the pores [1,35] and provide additional energy to open new pores [36]. Effectively, as shown above, there is an optimum shear rate and, accordingly, an optimum flow rate for cell permeabilization. The reason for this must be the nonlinear response of the cell to this linear stimulus. We argue that as the plasma membrane is the main barrier to overcome, the cause ought to be lipid ensemble centered. A common nonlinear phenomenon in lipid membranes is the existence of structural phase transitions, which so far have been rarely considered [37–39]. Previous studies have already shown that the lipid chain order parameter is decreased upon shear flow [40]. Recently, broad order–disorder transitions in HeLa membranes have been reported [41]. We hypothesize that a shift in the lipid membrane's phase transition on the temperature axis is caused by shear forces, effectively enlarging the membrane tension, as described in [31]. Thus, membrane fluidity (or, more generally, the phase state) is altered. For instance, De Haas et al. showed a phase transition in lipid membranes that appears at

low shear rates [42], which agrees well with our findings in the regime of mild shear in the order of $\dot{\gamma} = 30$–60 1/s.

Employing additional surface acoustic waves enhances the efficacy of permeabilization and enables dye uptake even at low flow rates, although it is not limited to low flow rates. We found that it is governed by a maximum ratio of the horizontal flow rate and the applied power, as reported earlier for mixing [20]. For too high powers, cell death is promoted. Furthermore, we found an optimum SAW cycle duration of $t_{SAW} = 2$ min, which is closely related with the contact time of maximum uptake in pure shear flow.

Moreover, variation in the molecule size of the model drug could be used to challenge the size of the formed pores and the application potential of this method. It is certainly not limited to small molecular sizes and does not end at sizes of sugars and proteins. We could show a significant amount of uptake of proteins, but did not test this further.

To quantitatively summarize, we show an effective uptake enhancement by SAW-mediated delivery compared to static incubation of about $f_C = 18$ for calcein. Further experiments suggest that this is not the limit, but rather that doubling t_{SAW} would result in a doubling of $f_C = 2 \cdot 18 = 36$. For FITC–dextran and eGFP, the according enhancement factors are $f_{FITC} \approx 3$ and $f_{eGFP} \approx 6$, respectively.

Future studies could contain upgraded and optimized setups to better control the dwell time distribution, e.g., by multiple traps connected in series, or by modulation of the amplitude with a lower frequency. This might increase the uptake, especially if the chosen frequency matches the mechanical resonance frequency of the whole cell. Overall, the SAW stimulated uptake in a microfluidic setup served as a new method for the screening of agent libraries, with high potential for further development.

Supplementary Materials: The following are available online at https://www.mdpi.com/article/10.3390/pr9060913/s1, Figure S1: Uptake as function of the flow rate for different corrections, Figure S2: Z-scan PIV measurements of the active SAW coupling into the microchannel.

Author Contributions: Conceptualization, C.W., U.L., E.W. and A.W.; methodology, A.K. and F.L.S.; software, F.L.S.; validation, C.W., A.K. and F.L.S.; formal analysis, A.K. and F.L.S.; investigation, C.W., U.L., A.K. and F.L.S.; resources, E.W. and A.W.; data curation, A.K. and F.L.S.; writing—original draft preparation, A.K., F.L.S. and C.W.; writing—review and editing, A.K. and C.W.; visualization, A.K., F.L.S. and C.W.; supervision, C.W.; project administration, C.W.; funding acquisition, C.W., U.L., E.W. and A.W. All authors have read and agreed to the published version of the manuscript.

Institutional Review Board Statement: Not applicable.

Informed Consent Statement: Not applicable.

Data Availability Statement: Data available on request due to restrictions.

Conflicts of Interest: The authors declare no conflict of interest.

References

1. Stewart, M.P.; Langer, R.; Jensen, K.F. Intracellular Delivery by Membrane Disruption: Mechanisms, Strategies, and Concepts. *Chem. Rev.* **2018**, *118*, 7409–7531. [CrossRef]
2. Gehl, J. Electroporation: Theory and methods, perspectives for drug delivery, gene therapy and research. *Acta Physiol. Scand.* **2003**, *177*, 437–447. [CrossRef]
3. Weaver, J.C. Electroporation of cells and tissues. *IEEE Trans. Plasma Sci.* **2000**, *28*, 24–33. [CrossRef]
4. Weaver, J.C.; Chizmadzhev, Y.A. Theory of electroporation: A review. *Bioelectrochem. Bioenergy* **1996**, *41*, 135–160. [CrossRef]
5. Rubinsky, B. Irreversible electroporation in medicine. *Technol. Cancer Res. Treat.* **2007**, *6*, 255–259. [CrossRef] [PubMed]

6.   Scheffer, H.J.; Nielsen, K.; De Jong, M.C.; Van Tilborg, A.A.J.M.; Vieveen, J.M.; Bouwman, A.; Meijer, S.; Van Kuijk, C.; Van Den Tol, P.; Meijerink, M.R. Irreversible electroporation for nonthermal tumor ablation in the clinical setting: A systematic review of safety and efficacy. *J. Vasc. Interv. Radiol.* **2014**, *25*, 997–1011. [CrossRef] [PubMed]

7.   Mitragotri, S. Healing sound: The use of ultrasound in drug delivery and other therapeutic applications. *Nat. Rev. Drug Discov.* **2005**, *4*, 255–260. [CrossRef]

8.   Lentacker, I.; De Cock, I.; Deckers, R.; De Smedt, S.C.; Moonen, C.T.W. Understanding ultrasound induced sonoporation: Definitions and underlying mechanisms. *Adv. Drug Deliv. Rev.* **2014**, *72*, 49–64. [CrossRef]

9.   Sheikh, S.; Pallagatti, S.; Singh, B.; Puri, N.; Singh, R.; Kalucha, A. Sonoporation, a redefined ultrasound modality as therapeutic aid: A review. *J. Clin. Exp. Dent.* **2011**, *3*, 228–234. [CrossRef]

10.   Mehier-Humbert, S.; Bettinger, T.; Yan, F.; Guy, R.H. Plasma membrane poration induced by ultrasound exposure: Implication for drug delivery. *J. Control. Release* **2005**, *104*, 213–222. [CrossRef]

11.   Belling, J.N.; Heidenreich, L.K.; Tian, Z.; Mendoza, A.M.; Chiou, T.-T.; Gong, Y.; Chen, N.Y.; Young, T.D.; Wattanatorn, N.; Park, J.H.; et al. Acoustofluidic sonoporation for gene delivery to human hematopoietic stem and progenitor cells. *Proc. Natl. Acad. Sci. USA* **2020**, *117*, 10976–10982. [CrossRef]

12.   Hanasaki, I.; Walther, J.H.; Kawano, S.; Koumoutsakos, P. Coarse-grained molecular dynamics simulations of shear-induced instabilities of lipid bilayer membranes in water. *Phys. Rev. E* **2010**, *82*, 051602. [CrossRef]

13.   Hallow, D.M.; Seeger, R.A.; Kamaev, P.P.; Prado, G.R.; LaPlaca, M.C.; Prausnitz, M.R. Shear-induced intracellular loading of cells with molecules by controlled microfluidics. *Biotechnol. Bioeng.* **2008**, *99*, 846–854. [CrossRef] [PubMed]

14.   Ramesan, S.; Rezk, A.R.; Dekiwadia, C.; Cortez-Jugo, C.; Yeo, L.Y. Acoustically-mediated intracellular delivery. *Nanoscale* **2018**, *10*, 13165–13178. [CrossRef]

15.   Ramesan, S.; Rezk, A.R.; Yeo, L.Y. High frequency acoustic permeabilisation of drugs through tissue for localised mucosal delivery. *Lab Chip* **2018**, *18*, 3272–3284. [CrossRef] [PubMed]

16.   Hodgson, R.P.; Tan, M.; Yeo, L.; Friend, J. Transmitting high power rf acoustic radiation via fluid couplants into superstrates for microfluidics. *Appl. Phys. Lett.* **2009**, *94*, 024102. [CrossRef]

17.   Sritharan, K.; Strobl, C.J.; Schneider, M.F.; Wixforth, A.; Guttenberg, Z. Acoustic mixing at low Reynold's numbers. *Appl. Phys. Lett.* **2006**, *88*, 054102. [CrossRef]

18.   Wixforth, A. Acoustically Driven Programmable Microfluidics for Biological and Chemical Applications. *J. Lab. Autom.* **2006**, *11*, 399–405. [CrossRef]

19.   Dean, S.; Rathgeber, A.; Wassermeier, M.; Wixforth, A. Acoustic 'Distributed Source' Mixing of Smallest Fluid Volumes. *J. ASTM Int.* **2005**, *2*, 12829. [CrossRef]

20.   Westerhausen, C.; Schnitzler, L.; Wendel, D.; Krzysztoń, R.; Lächelt, U.; Wagner, E.; Rädler, J.; Wixforth, A. Controllable Acoustic Mixing of Fluids in Microchannels for the Fabrication of Therapeutic Nanoparticles. *Micromachines* **2016**, *7*, 150. [CrossRef]

21.   Frommelt, T.; Kostur, M.; Wenzel-Schäfer, M.; Talkner, P.; Hänggi, P.; Wixforth, A. Microfluidic mixing via acoustically driven chaotic advection. *Phys. Rev. Lett.* **2008**, *100*, 1–4. [CrossRef] [PubMed]

22.   Streibl, M.; Wixforth, A.; Kotthaus, J.P.; Govorov, A.O.; Kadow, C.; Gossard, A.C. Imaging of acoustic charge transport in semiconductor heterostructures by surface acoustic waves. *Appl. Phys. Lett.* **1999**, *75*, 4139–4141. [CrossRef]

23.   Xia, Y.; Whitesides, G.M. Soft Lithography. *Annu. Rev. Mater. Sci.* **1998**, *28*, 153–184. [CrossRef]

24.   Illes, B.; Hirschle, P.; Barnert, S.; Cauda, V.; Wuttke, S.; Engelke, H. Exosome-Coated Metal—Organic Framework Nanoparticles: An Efficient Drug Delivery Platform. *Chem. Mater.* **2017**, *29*, 8042–8046. [CrossRef]

25.   Maier, K.; Wagner, E. Acid-Labile Traceless Click Linker for Protein Transduction. *J. Am. Chem. Soc.* **2012**, *134*, 10169–10173. [CrossRef]

26.   Thielicke, W.; Stamhuis, E.J. PIVlab—Towards User-friendly, Affordable and Accurate Digital Particle Image Velocimetry in MATLAB. *J. Open Res. Softw.* **2014**, *2*. [CrossRef]

27.   Clarke, M.S.F.; McNeil, P.L. Syringe loading introduces macromolecules into living mammalian cell cytosol. *J. Cell Sci.* **1992**, *102 Pt 3*, 533–541. [CrossRef]

28.   Dean, W.R. Fluid Motion in a Curved Channel. *Proc. R. Soc. A Math. Phys. Eng. Sci.* **1928**, *121*, 402–420. [CrossRef]

29.   Sharei, A.; Zoldan, J.; Adamo, A.; Sim, W.Y.; Cho, N.; Jackson, E.; Mao, S.; Schneider, S.; Han, M.-J.; Lytton-Jean, A.; et al. A vector-free microfluidic platform for intracellular delivery. *Proc. Natl. Acad. Sci. USA* **2013**, *110*, 2082–2087. [CrossRef]

30.   Geislinger, T.M.; Franke, T. Hydrodynamic lift of vesicles and red blood cells in flow—From Fåhræus & Lindqvist to microfluidic cell sorting. *Adv. Colloid Interface Sci.* **2014**, *208*, 161–176. [CrossRef]

31.   De Haas, K.H.; Blom, C.; van den Ende, D.; Duits, M.H.G.; Mellema, J. Deformation of giant lipid bilayer vesicles in shear flow. *Phys. Rev. E* **1997**, *56*, 7132–7137. [CrossRef]

32.   Debye, P.; Hückel, E. Zur Theorie der Elektrolyte. I. Gefrierpunktserniedrigung und verwandte Erscheinungen. *Phys. Z.* **1923**, *24*, 305.

33.   Evans, E.; Heinrich, V.; Ludwig, F.; Rawicz, W. Dynamic tension spectroscopy and strength of biomembranes. *Biophys. J.* **2003**, *85*, 2342–2350. [CrossRef]

34.   Tamba, Y.; Ariyama, H.; Levadny, V.; Yamazaki, M. Kinetic Pathway of Antimicrobial Peptide Magainin 2-Induced Pore Formation in Lipid Membranes. *J. Phys. Chem. B* **2010**, *114*, 12018–12026. [CrossRef] [PubMed]

35. Akimov, S.A.; Volynsky, P.E.; Galimzyanov, T.R.; Kuzmin, P.I.; Pavlov, K.V.; Batishchev, O.V. Pore formation in lipid membrane II: Energy landscape under external stress. *Sci. Rep.* **2017**, *7*, 12509. [CrossRef]

36. Blicher, A.; Wodzinska, K.; Fidorra, M.; Winterhalter, M.; Heimburg, T. The temperature dependence of lipid membrane permeability, its quantized nature, and the influence of anesthetics. *Biophys. J.* **2009**, *96*, 4581–4591. [CrossRef]

37. Petronilli, V.; Miotto, G.; Canton, M.; Brini, M.; Colonna, R.; Bernardi, P.; Di Lisa, F. Transient and Long-Lasting Openings of the Mitochondrial Permeability Transition Pore Can Be Monitored Directly in Intact Cells by Changes in Mitochondrial Calcein Fluorescence. *Biophys. J.* **1999**, *76*, 725–734. [CrossRef]

38. Beattie, G.M.; Crowe, J.H.; Lopez, A.D.; Cirulli, V.; Ricordi, C.; Hayek, A. Trehalose: A Cryoprotectant That Enhances Recovery and Preserves Function of Human Pancreatic Islets After Long-Term Storage. *Diabetes* **1997**, *46*, 519–523. [CrossRef] [PubMed]

39. Van Die, I.M.; Bergmans, H.E.N.; Hoekstra, W.P.M. Transformation in Escherichia coli: Studies On The Role Of The Heat Shock In Induction Of Competence. *Microbiology* **1983**, *129*, 663–670. [CrossRef]

40. Yamamoto, K.; Ando, J. Endothelial cell and model membranes respond to shear stress by rapidly decreasing the order of their lipid phases. *J. Cell Sci.* **2013**, *126*, 1227–1234. [CrossRef]

41. Färber, N.; Westerhausen, C. Broad lipid phase transitions in mammalian cell membranes measured by Laurdan fluorescence spectroscopy. *Rev. Sci. Rep.* **2021**. [CrossRef]

42. De Haas, K.H.; Blom, C.; van den Ende, D.; Duits, M.H.G.; Haveman, B.; Mellema, J. Rheological Behavior of a Dispersion of Small Lipid Bilayer Vesicles. *Langmuir* **1997**, *13*, 6658–6668. [CrossRef]